A Computational Framework for Coating Fatigue Analysis of Wind Turbine Blades Due to Rain Erosion

Weifei Hu[1,2*], **Weiyi Chen**[1,2], **Xiaobo Wang**[2], **Zhiyu Jiang**[3], **Yeqing Wang**[4], **Amrit Verma**[5], **Julie Teuwen**[5]

[1] State Key Laboratory of Fluid Power and Mechatronic Systems, Zhejiang University, Hangzhou 310027, China

[2] School of Mechanical Engineering, Zhejiang University, Hangzhou 310027, China

[3] Department of Engineering Sciences, University of Agder, N-4898 Grimstad, Norway

[4] Department of Mechanical and Aerospace Engineering, Syracuse University, Syracuse, NY 13244, USA

[5] Faculty of Aerospace Engineering, Delft University of Technology, Delft, The Netherlands

*Corresponding author: Weifei Hu (weifeihu@zju.edu.cn)

Abstract

The rain-induced fatigue damage in the wind turbine blade coating has attracted increasing attention owing to significant repair and maintenance costs. The present paper develops an improved computational framework for analyzing the wind turbine blade coating fatigue induced by rain erosion. The paper first presents an extended stochastic rain field simulation model that considers different raindrop shapes (spherical, flat, and spindle), raindrop sizes, impact angles, and impact velocities. The influence of these raindrop characteristics on the impact stress of the blade coating is investigated by a smoothed particle hydrodynamic approach. To address the expensive computational time, a stress interpolation method is proposed to calculate the impact stress of all raindrops in a random rain event. Furthermore, coating fatigue analysis is performed by including the fatigue crack initiation in the incubation period and the fatigue crack propagation in the mass-loss-rate increasing period due to raindrop impact. Finally, the proposed computational framework is verified by comparing the estimated fatigue life with those obtained in literature. The results from the study show that by incorporating the statistics of rainfall data, the proposed framework could be used to calculate the expected fatigue life of the blade coating due to rain erosion.

Keywords: wind turbine blade, rain erosion, raindrop impact, fatigue analysis, crack propagation, smoothed particle hydrodynamic

1 INTRODUCTION

Wind turbine blades (WTBs), especially at tip sections, are frequently exposed to impacts from high-relative-speed objects such as rain, atmospheric particles, hail, and sand during the service life. These impacts may induce erosion damage at the blade leading edge, thereby reducing

the aerodynamic performance and power output of wind turbines. In addition, such issues require regular maintenance and repair, causing an increase in the cost of energy. The issue of leading edge erosion (LEE) of WTBs is becoming even more crucial as wind turbines continue to grow in both hub-height and rotor diameter and are associated with large tip speeds.

Among the above-stated impacts from relatively high-speed objects, raindrop impact is one of the most important factors that contributes to LEE of WTBs. Traditionally, there are two approaches utilized for analyzing the rain erosion problem, the impact approach (e.g., [1]) or the energetic approach (e.g., [2]). The former approach first calculates the impact pressure using either explicit formulas, e.g., the water-hammer equations [3, 4], or the expensive computational fluid dynamic (CFD) methods (e.g. [5]), then carries out the transient stress analysis by applying the pressure force on the finite element model of a WTB (e.g., [5]). Although it is less computationally intensive to calculate pressure by the explicit water-hammer equations, the following assumptions are made: (1) the impact occurs in one dimension and (2) the impact solid is a perfect rigid body [3], which do not realistically represent raindrop impacts. In addition, it is difficult to take into the account the fluid-solid interaction during raindrop impact by sequentially calculating the impact pressure and the transient stress. The energetic approach attempts to relate the erosion to mechanical properties of the impact body based on the kinetic energy transmitted. Although this approach can potentially avoid simplifications (e.g., the impact effects are independent of each raindrop and the shape of raindrops is a perfect sphere), it is difficult to quantify the total transferred energy from the stochastic rain field to the WTB.

A high-fidelity simulation of rain events is essential for accurately predicting the erosion process. However, as rain events are complex natural phenomena, it is challenging to simulate them realistically due to varying raindrop sizes, shapes, and speeds. By integrating the micro-

structural properties of rain, i.e., raindrop sizes and spatial distribution, a stochastic rain texture model is developed to generate three-dimensional rain fields by Amirzadeh et al. [5]. In this model, the raindrops with perfectly spherical shapes in the simulated rain event are assumed to be distributed randomly in the spatial domain. However, the raindrops in the falling rain have a complex mutual interaction with their neighbors, which causes varied velocity, sizes, and shapes, as well as inflation, destabilization and ultimate fragmentation during the falling [6]. For example, different raindrop shapes exist, e.g., spherical, semi-oblate, and parachute forms for raindrops diameter less than 2-mm, between 2 and 5 mm, and larger than 5 mm, respectively [7]. The raindrop shapes are highly dynamic in response to coalescence or fragmentation and to aerodynamic forces (e.g., distorting the raindrop to a burger-bun-like shape [8]). Additionally, the terminal velocity, i.e., the highest velocity attainable by the raindrop falling through the air, is affected by raindrop mass, humidity, temperature, and orography, as well as wind. Thus, it is a very challenging task to simulate a realistic stochastic rain field considering all the aforementioned factors.

Calculations of raindrop impact pressure and/or impact stress is an important step before evaluating the fatigue damage due to rain erosion. Due to its explicit formulation, the water hammer pressure is viewed in literature (e.g., [7-11]) as a preliminary metric to evaluate the raindrop impact force on solid surface. To consider the influence of the stress wave reflections, Eisenberg et al. corrected the water hammer pressure by multiplying a term including impedance of the substrate and the coating material [9]. By integrating the stochastic rain texture model and the raindrop impact pressure profiles [5], Amirzadeh et al. further conducted the transient stress analysis in a composite WTB using finite element analysis, although the stress analysis is limited to the time period before which surface roughening starts to appear (i.e., the incubation period)

[11]. To the authors' knowledge, there is still a lack of an efficient and accurate computational model that well reveals the complex fatigue mechanism for crack propagation induced by the raindrop impact.

In the fatigue analysis, very little research has considered the influence of complex rain-induced stress on the fatigue life-cycle of WTB coating, including the incubation period, the mass-loss-rate (MLR) increasing period, and the placid period [12] , as shown in Fig. 1. The WTB coating fatigue damage is initiated in the incubation period and increased rapidly in the MLR increasing period. In the incubation period, the coating surface is smoother without obvious pits and cracks, and there is no obvious observable mass loss due to raindrop erosion. The damage in this period is mainly attributed to fatigue of the solid material under direct deformation and stress wave propagation [13, 14]. As the erosion process continues and the surface roughness is increased in the MLR increasing period, the lateral jetting and hydraulic penetration produce large shear stress on the surface and the fatigue crack opening causing the increased MLR [15]. In the placid period, as the surface roughness is severely increased, liquid material accumulates on the surface and reduces the impact damage of the oncoming raindrops resulting in a decreased MLR in this period [5]. It is important to correctly estimate the time lengths of the former two periods before the aerodynamic and structural performance of WTBs are significantly degraded. Although several studies have investigated the WTB rain erosion considering the incubation period (e.g., [8, 9, 11]), very few have considered both the incubation period and the MLR increasing period. For example, the Miner's rule has been often applied to estimate the fatigue damage by a simple linear accumulation of fatigue damage due to each stress cycle in the incubation period (e.g., [8-11, 16]). Eisenberg et al. [9] derived an analytic wind turbine LEE model and found that fatigue damage rate is proportional to the impact velocity and rain intensity to the power of 6.7 and 2/3,

111 respectively. However, in this model, the rain consists of only droplets of the median diameter
112 under a certain rain intensity, and the fatigue calculation only considers the crack initiation during
113 the incubation period.

114 In view of existing challenges, the current paper presents a comprehensive computational
115 framework (Fig. 2) for analyzing the WTB coating fatigue induced by raindrop impact. The
116 framework investigates the WTB coating fatigue life and includes three parts: 1) an extended
117 stochastic rain field simulation, 2) raindrop-impact stress calculation, and 3) coating fatigue
118 analysis, as schematically shown in Fig. 3. The novelties of this work are three-fold:

119 1) An extended stochastic rain field simulation model considering the varied raindrop shapes
120 (spherical, flat, and spindle) and realistic raindrop size and distribution based on historical rain
121 data;
122 2) An efficient and accurate method to calculate the raindrop-impact stress under a stochastic rain
123 event using the smooth particle hydrodynamics (SPH) and a stress interpolation scheme;
124 3) Coating fatigue analysis including the incubation period and the MLR increasing period due
125 to impact of raindrops.

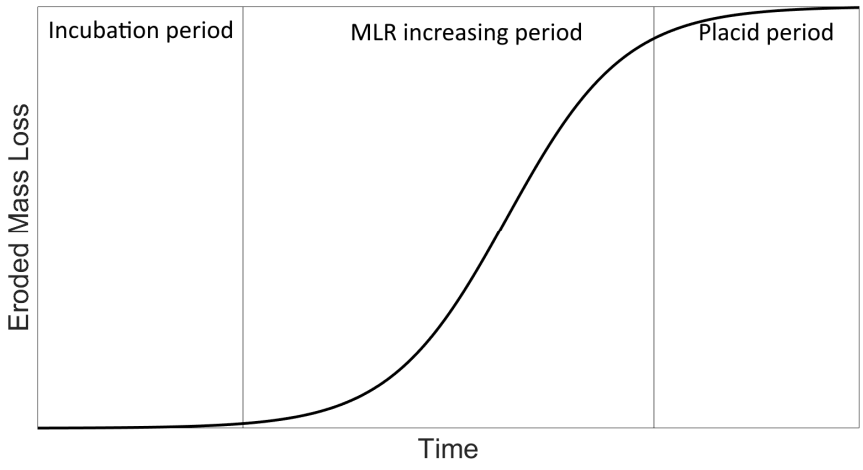

126

127 **Figure 1** Eroded mass loss vs. time in rain erosion. Adapted from Springer and Yang(1975) [12]

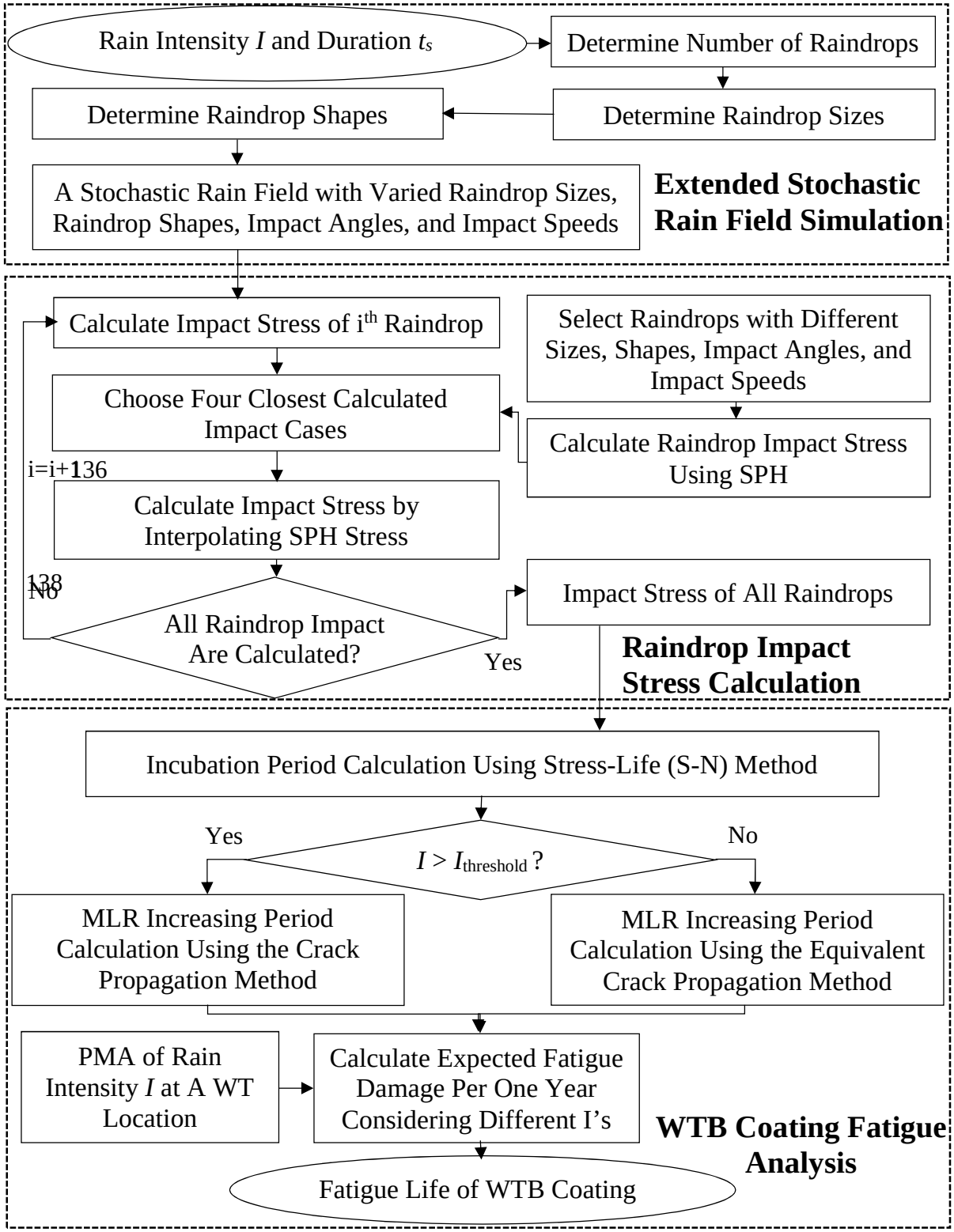

Figure 2 The computational framework of wind turbine blade (WTB) coating fatigue due to rain erosion.

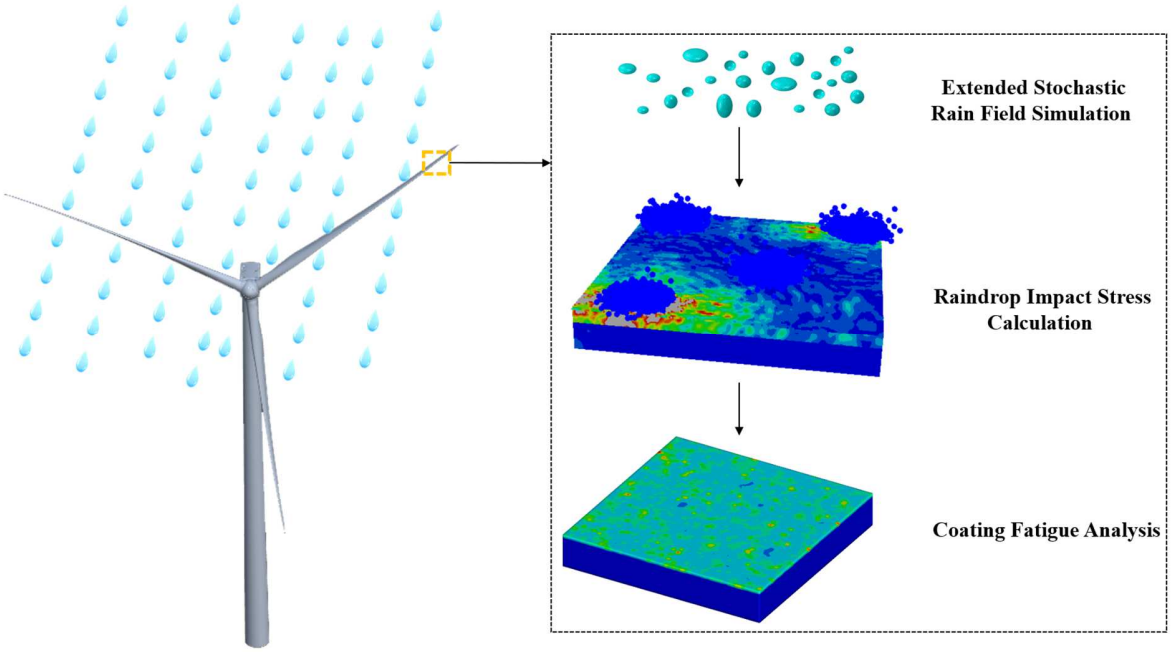

Figure 3 Schematic diagram of wind turbine blade coating fatigue induced by raindrop impact.

The remainder of the paper proceeds as follows. Section 2 presents the detailed methodologies of the proposed computational framework. Section 3 provides a case study using the framework, followed by the results and discussion in Section 4. Section 5 gives the concluding remarks, limitations, and future work.

2 METHODOLOGIES

Different from the existing simulated rain fields which only include perfectly spherical raindrops (e.g., by the methods in [5]), the extended stochastic rain fields herein consists of spherical and elliptical raindrop shapes according to the work in [17]. Since the raindrop impact velocity is dominated by wind turbine rotation [5, 18], we consider the angle between the falling raindrops and the rotating blade as the impact angle, instead of using the commonly assumed vertical hitting angle of 90 degrees [11, 16]. The raindrop impact stress is calculated using SPH and the FEA methods. To simulate the coating erosion in the life cycle of the blade, the coating

fatigue analysis includes both fatigue incubation and crack propagation periods.

2.1 Extended Stochastic Rain Field Simulation

The extended stochastic rain field model is based on the stochastic rain texture model described in [5], and further considers different raindrop impact speeds, impact angles, sizes of raindrops, and shapes of raindrops in the simulated rain fields. The simulated stochastic rain field consists of three key components, including the number of raindrops in unit volume, the distribution of the size of raindrops, and the spatial distribution of raindrops with varying shapes in the simulated volume. The number of raindrops in unit volume V, $N(V)$, follows a Poisson distribution expressed as [5]:

$$P\left(N\left(V\right)=k\right)=\frac{\left(\lambda V\right)^{k}e^{-\lambda V}}{k!} \tag{1}$$

where λ is the expected number of raindrops per unit volume, and $P(N(V) = k)$ is the probability of having k raindrops in volume V. Based on the relationship between the volume of water in air and the rain intensity suggested by Best [19], the expected number λ of raindrops per unit volume can be described by a power-law relationship with the rain intensity following Amirzadeh et al. [5]

$$\lambda = 48.88 I^{0.15} \tag{2}$$

where I is the rain intensity in mm h^{-1}. We use Best's drop size distribution [19] to connect the rain intensity with the distribution of the size of raindrops since it closely matches the experimental data [5]. The cumulative distribution function F of the raindrop size (e.g., diameter) is expressed as:

$$F = 1-\exp\left[-\left(\frac{d}{1.3I^{0.232}}\right)^{2.25}\right] \tag{3}$$

where d is the raindrop diameter in mm and I is the rain intensity in mm h^{-1}.

Due to surface tension and external forces (e.g., aerodynamic force and gravity force), raindrops normally have varying shapes when impacting WTBs. In this paper, the equilibrium shape of raindrops is described by the axis ratio α, a ratio of the minor axis to the major axis of the ellipse [17]. In the measurements by Beard et al., the axis ratio α of a raindrop is found to have a linearly decreasing relationship with the equivalent spherical radius r_0 (r_0 is in the range of 0.5 – 4.5 mm), which is expressed as [17]

$$\alpha = 1.030 - 0.124 r_0 \tag{4}$$

To address the varying raindrop shapes in a rain event, the equivalent spherical radii r_0 of the simulated raindrops are obtained based on the Best's drop size distribution (Eq. 3). Three types of raindrop shapes are considered, perfect sphere, flat ellipsoid, and spindle ellipsoid. The flat-ellipsoid raindrops have the longest axis in horizontal plan, while the spindle-ellipsoid raindrops have the longest axis perpendicular to the horizontal plan. The horizontal cross-sectional area of both flat and spindle raindrops is assumed to be a circle, and the vertical cross-sectional area is an ellipse. The axis ratio of the minor axis to the major axis of the ellipse is calculated by Eq. (4). For the raindrops having the same equivalent spherical radius, their volumes are the same although their shapes may be different. In the experiments of McTaggart-Cowan and List (1975) [17, 20], raindrop collisions were used to classify three predominate breakup types which is neck (27%), sheet (55%) and disk (18%). As the raindrop shapes after collision of these three types are comparable to the flat ellipsoid, spindle ellipsoid, and perfect sphere [17, 20], we select the same probability of occurrence for the three raindrop shapes to be 27%, 55%, and 18%, respectively, in the simulated stochastic rain event, as shown in Fig. 4.

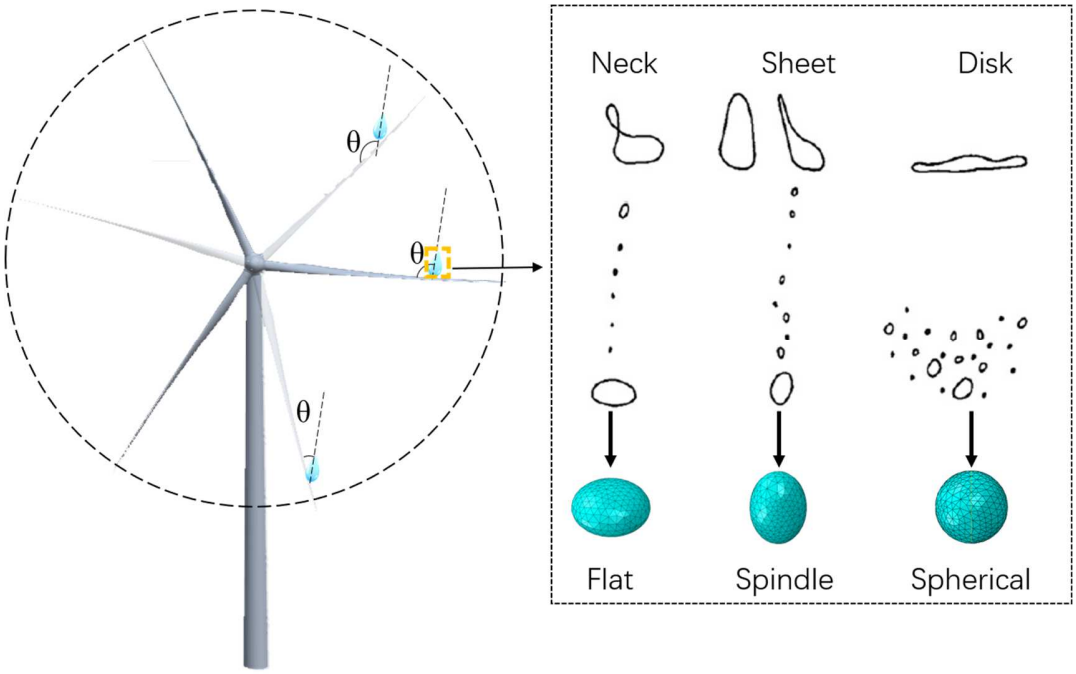

207

208 **Figure 4** Schematic diagram of raindrop shape and impact angle. The flat, spindle, and spherical
209 raindrops correspond to the three predominate breakup types (i.e., neck 27%, sheet 55%, and
210 disk 18% from the reference [17]).

211 Due to the WTB rotation and complex weather condition (e.g., wind effect), raindrops could
212 impact the WTB at different angles (Fig. 4). The normal and tangential loads exerted due to
213 perpendicular impact and inclined impact, respectively, could create different stress distribution in
214 the blade coating. Thus, this paper further considers the inclined impact angle between the rotating
215 blade and the falling raindrops. While the impact angle could range from 0 to 180° (denoted as [0,
216 180°] herein) as demonstrated in Fig. 4, it is assumed to follow a uniform distribution from 0 to
217 90° considering the symmetric impacting effect between the ranges of [0, 90°] and [90°, 180°].

218 As a raindrop is falling, the air resistance applied on the raindrop approaches to its gravity,
219 which may result in a constant terminal speed. For instance, the terminal speed of raindrops with
220 diameters larger than 3.5 mm through stagnant air is approximately 9 ms^{-1} [18, 21]. However, as

a result of the high relative speed between a rotating megawatt-scale WTB and the falling raindrops, raindrop impact speed at the tip of the blade could be 90-100 ms^{-1} [18]. In addition, the raindrops are considered as uniformly distributed in a tall-column volume. The height h of the column is calculated by the multiplication of the impact speed v and the duration T of the simulated rain event (i.e., $h = v \times T$), as also conducted by Amirzadeh et al. [5]. Given the statistical data of rainfall history at a wind turbine location (see Section 3 for instance), the probability mass function (PMF) of the rain intensity can be obtained and used to determine different rainfall hours per year for the coating fatigue life estimation in Section 2.3.

2.2 Method for Raindrop Impact Stress Calculation

The raindrop impact is simulated by the transient SPH using the FEA tool in ABAQUS/Explicit [11]. This SPH approach has three merits: (1) taking into the account of large deformation of raindrops during impact on the solid, (2) directly calculating the transient stress time series, and (3) characterizing the impact wave propagation in the FEA model.

2.2.1 Impact stress calculation of a single raindrop

The SPH approach is particularly effective to solve large deformation problems that can afford moderate computational cost, which is its key advantage over traditional FEA and the coupled Eulerian-Lagrangian approaches. The former is not as accurate as SPH for large deformation analysis, while the latter is usually more computationally expensive than SPH. Detailed theory and application of SPH can be found in literature [22-24]. Keegan et al. [25] utilized the SPH method to simulate the effects of rain and hail on the coating materials of wind turbines. The SPH method is coupled with traditional FEA to study the fluid-structural interaction between the raindrop and the WTB (e.g., Astrid et al. [26] and Verma et al. [27]).

To reflect the aforementioned complexity of raindrops in a rain event, herein the SPH analysis is first applied to investigate single raindrop impact considering different raindrop sizes, raindrop shapes, impact speeds, and impact angles. Specifically, we conduct varying single-raindrop impact cases considering 9 raindrop sizes (equivalent diameter d = 1, 2, 3, 4, 5, 6, 7, 8, 9 mm), 3 raindrop shapes (flat, spindle, spherical), 6 impact angles (θ = 15°, 30°, 45°, 60°,75°, 90°), and 5 impact speeds (70 ms^{-1}, 80 ms^{-1}, 90 ms^{-1}, 100 ms^{-1}, 110 ms^{-1}). Detailed results and discussion are seen in Section 4.2. The von Mises stress due to multiple-raindrops impact in a simulated rain field is further calculated based on the interpolation of the von Mises stress results of the single-raindrop impact cases, as explained in the following section.

2.2.2 Impact stress calculation under a random rain event

In a real rain event, a significant number of raindrops with varied sizes, shapes, and impact speeds and angles are randomly impacting on WTBs. For a single raindrop impact simulation by SPH, it costs 2 hours using a computer (Intel(R) Core(TM) i7-9700H CPU @ 3.00 GHz Processor, Memory (RAM) 32 GB, 64-bit Windows Operating System). Thus, it is not practical to conduct SPH simulation for all raindrops in a rain event. Instead, an interpolation method is proposed to efficiently obtain the impact stress due to varied raindrop sizes, shapes, and impact speeds and angles. The method utilizes pre-calculated impact stress from the single-raindrop impact cases. Detailed steps are explained as follows:

Step 1: Create a stochastic rain field by the method presented in Section 2.1 given a rain intensity and a rain duration.

Step 2: Obtain the impact stress of a random raindrop by interpolating the SPH impact stress from the single-raindrop impact cases in Section 2.2.1. After identifying the size, shape, and the

265 impact angle and speed of the random raindrop, a circular domain with the impact point as the
266 center and 10 times of the raindrop equivalent diameter as the radius is considered as the area
267 influenced by the raindrop impact [11]. Then, choose the same type of raindrop shape, and
268 interpolate the stress in this circular area according to the stress results of the calculated impact
269 cases that have the closest raindrop diameter, impact angle, and impact speed.

270 **Step 3:** Repeat Step 2 for calculating the impact stress due to the other random raindrops.
271 Since the time interval between two consecutive raindrops impact is almost three orders of
272 magnitude longer than the time required for the stress wave generated by a single raindrop impact
273 to disappear [11], we assume that the stress waves from different single-raindrop impacts will not
274 interact with each other.

275 Through the above steps, the complex stress state under a stochastic rain field can be
276 calculated and used for the coating fatigue analysis as follows.

277 **2.3 Coating Fatigue Analysis**

278 Herein we first use the traditional alternating stress (S) versus the number of cycles to failure
279 (N), here defined as the stress life (S-N) method to calculate the fatigue life during the incubation
280 period, then propose a fatigue crack propagation method to calculate the fatigue life during the
281 MLR increasing period.

282 **2.3.1 Fatigue analysis for the incubation period**

283 The traditional S-N method has been widely used to calculate the fatigue life during the
284 incubation period [11, 28, 29]. The S-N curve formula is expressed as：

285 $$\sigma_a = \sigma_f (N_f)^b \tag{5}$$

where σ_f is the fatigue strength coefficient (FSC), and b is the fatigue strength exponent (FSE), N_f is the number of allowable cycles under a stress amplitude σ_a. According to the fatigue experiments in [30], the values of σ_f and b in Eq.(5) are 83.3MPa and −0.117, respectively, for the epoxy coating used in this paper.

It is worth noting that the S-N curve formula differs at different stress ratios R which equal the ratio of the minimum cyclic stress to the maximum cyclic stress (i.e., $R = \sigma_{\min} / \sigma_{\max}$). However, due to the lack of experimental data for fatigue of the coating material under different stress ratios, a single S-N curve based on the fatigue experiments in [30] is used and the stress amplitudes are corrected according to the Goodman's equation [11]:

$$\sigma_a^{'} = \frac{\sigma_a UTS}{UTS - \sigma_m} \tag{6}$$

where $\sigma_a^{'}$ is the corrected amplitude, σ_m is the mean stress, and *UTS* is the ultimate tensile strength. The *UTS* of the epoxy material (*UTS* = 73.3MPa) from [30] is used in this paper. Substituting the σ_a in Eq. (5) by $\sigma_a^{'}$, the number of allowable stress cycles N_f can be calculated as

$$N_f = \left(\frac{\sigma_a^{'}}{\sigma_f} \right)^{1/b} \tag{7}$$

In Eq. (7), the cyclic stress should be a constant-amplitude cyclic stress, but the actual impact stress has varied stress amplitudes due to the randomness of raindrop impact. In order to have cycle-by-cycle fatigue analysis, a simple-range counting method [31] is applied to count all the half cycles, i.e., the local maximum (minimum) stress and the neighboring minimum

(maximum) stress are selected to constitute a half stress cycle. In this way, the complex stress curve is split into half-cyclic stresses with varying constant-amplitudes and the N_f in Eq. (7) is calculated for each half-cycle. Different from the rainflow cycle counting that breaks the stress cycle sequence, the simple-range counting method could sequentially calculate fatigue damage for each half-cycle. As a result, the fatigue damage D under half-cyclic stresses is linearly accumulated based on the Miner's rule

$$D=\sum_i \frac{0.5}{N_f^i} \tag{8}$$

The fatigue life during the incubation period is then calculated as

$$t_{\text{incubation}} = \frac{t_s}{D_s} \tag{9}$$

where t_s is the duration of the simulated rain and D_s is the damage accumulated over time t_s.

2.3.2 Fatigue analysis for the mass-loss-rate increasing period

The MLR increasing period starts at the end of the incubation period when the surface roughness increases severely [5]. According to the crack propagation law [32], we use the obtained raindrop impact stress from Section 2.2.2 to calculate the crack depth, and use a crack-propagation stability criterion to calculate the fatigue life of the coating during the MLR increasing period when the rain intensity is larger than a threshold. When the rain intensity is smaller than or equal to the threshold, the computational time using this traditional crack propagation method is increased significantly. For example, using the traditional crack propagation method, the computer in this study will take approximately 179.67 days to calculate a fatigue life of 11462 hours when the rain intensity equals to 5 mm h^{-1}. To overcome the computational burden, an equivalent crack

propagation method is proposed for estimating the total crack propagation time by calculating the equivalent stress range, when the rain intensity is smaller than a threshold. In this study, the rain intensity threshold is selected to be 10 mm h^{-1} based on our current affordable computational time. The proposed equivalent crack propagation method significantly reduces the computational time when calculating fatigue life during the MLR increasing period. For instance, it only cost 1.7 minutes to simulate the same fatigue life when the rain intensity equals to 5 mm h^{-1}.

The crack propagation method is first explained. Fatigue crack propagation studies are performed with the cyclic-crack-tip stress state determined by a stress intensity factor range ΔK. According to the Paris law [32], the crack growth rate is expressed as:

$$\frac{da}{dN} = C(\Delta K)^m \tag{10}$$

where C and m are the basic parameters describing the fatigue crack growth performance of the material, obtained from the crack growth experiments. According to Brown's experimental results [33], the crack propagation test for the epoxy material (i.e., the gelcoat of a WTB) determines these parameters to be C=9.7 and m=0.08. Considering that the von Mises stress is used in the fatigue analysis (i.e., $R = \frac{\sigma_{min}}{\sigma_{max}} > 0$), the stress intensity factor range ΔK is expressed as [28, 29]

$$\Delta K = K_{\max} - K_{\min} \tag{11}$$

The calculation formula of stress intensity factor K is expressed as [28, 29]

$$K = Y\sigma\sqrt{\pi a} \tag{12}$$

Therefore, the maximum stress intensity factor $K_{\max}$ and the minimum stress intensity factor $K_{\min}$ can be expressed as $K_{\max} = Y\sigma_{\max}\sqrt{\pi a}$ and $K_{\min} = Y\sigma_{\min}\sqrt{\pi a}$, respectively. Y is a dimensionless parameter related to the shape of the crack. a is the crack depth.

346 For a constant amplitude stress and the number of stress cycles N is small, the change in crack
347 depth a is small and the stress intensity factor range ΔK is viewed as a constant. Thus the crack
348 growth rate (Eq. (10)) under a constant-amplitude cyclic stress can be considered as a constant. As
349 a result, the crack depth formula is approximately as

350 $$a = a_0 + \int_0^N C\left(\Lambda K\right)^m dN = a_0 + N \times C(\Delta K)^m \tag{13}$$

351 where N is the number of applied stress cycles and a_0 is the initial crack depth, which is selected
352 to be 12 μm according to the range of surface roughness (5 to 20 μm) used in [34]. This surface
353 roughness range is viewed as the indicator of the start of the MLR increasing period in this paper.

354 Since the stress time series have been split into half-cycle stresses, each half-cycle stress curve
355 is viewed as a constant amplitude stress with the number of stress cycles 0.5 (N = 0.5). The crack
356 depth a_{i+1} after one half-cycle stress cycle is calculated based on Eqs. (11) - (13)

357 $$a_{i+1} = a_i + 0.5 \times C\left[Y\left(\sigma_{\max} - \sigma_{\min}\right)\sqrt{\pi a_i}\right]^m \tag{14}$$

358 According to the elastic fracture criterion, when the maximum stress intensity factor $K_{\max}$ is
359 greater than the fracture toughness K_C , the crack extends in a rapid (unstable) manner without an
360 increase in load or applied energy [28]. Here the fracture toughness of the epoxy material is K_C =
361 0.59 MPa $m^{1/2}$ [33]. Here the relationship $K_{\max} > K_C$ is viewed as the first criterion indicating the
362 crack propagation has been completed. In addition, when the crack depth is greater than the coating
363 thickness, it also indicates that the crack propagation has been completed. By satisfying either the
364 aforementioned two criteria, the duration of the MLR increasing period t_{MLR} is obtained.

365 However, when the rain intensity is low, the time required for iteratively calculating the crack
366 depth (Eq. (14)) till the end of the crack propagation is significantly long due to the relatively small

impact stress. Herein for low rain intensity (i.e., I <= 10 mm h^{-1}), an average stress range $\Delta\sigma$ is first calculated as an equivalent constant-amplitude stress with the same applied number of cyclic stresses during the simulated rainfall time, which is based on the Paris formula. Then obtain the fatigue life based on accumulation of fatigue damage of multiple simulated times. Details of this equivalent crack propagation method are provided as follows.

Based on Eqs. (10) and (12), the number of allowable cyclic stress N_c can be calculated as:

$$N_c = \int_0^{N_c} dN = \int_{a_0}^{a_c} \frac{da}{C\left(Y\Delta\sigma\sqrt{\pi a}\right)^m} = \frac{1}{C\left(Y\Delta\sigma\sqrt{\pi}\right)^m} \int_{a_0}^{a_c} \frac{da}{a^{m/2}} \tag{15}$$

If $m \neq 2$

$$\int_{a_0}^{a_c} \frac{da}{a^{m/2}} = \frac{a_c^{\left(1-\frac{m}{2}\right)} - a_0^{\left(1-\frac{m}{2}\right)}}{-m/2+1} \tag{16}$$

If $m = 2$

$$\int_{a_0}^{a_c} \frac{da}{a} = \ln\left(\frac{a_c}{a_0}\right) \tag{17}$$

The calculation formula of fatigue life is derived as [28, 29]

$$N_c = \begin{cases} \dfrac{2}{(m-2)C\left(Y\Delta\sigma\sqrt{\pi}\right)^m}\left[a_0^{\left(1-\frac{m}{2}\right)} - a_c^{\left(1-\frac{m}{2}\right)}\right], & m \neq 2 \\ \dfrac{1}{C\left(Y\Delta\sigma\sqrt{\pi}\right)^m} \ln\left(\dfrac{a_c}{a_0}\right), & m = 2 \end{cases} \tag{18}$$

The parameters of the calculation formula for fatigue life (C, m, Y, a_0) are constant. Based on Eq.(18), the average stress range $\Delta\sigma$ of N number of varied-amplitude cyclic stress can be calculated as

$$\Delta\sigma = \begin{cases} \left\{ \dfrac{2}{N(m-2)C\left(Y\sqrt{\pi}\right)^m} \left[a_0^{\left(1-\frac{m}{2}\right)} - a^{\left(1-\frac{m}{2}\right)} \right] \right\}^{\frac{1}{m}}, & m \neq 2 \\ \left[\dfrac{1}{CN\left(Y\sqrt{\pi}\right)^m} \ln\left(\dfrac{a}{a_0}\right) \right]^{\frac{1}{m}}, & m = 2 \end{cases} \tag{19}$$

where N is the applied number of cyclic stress and a is the crack depth. By Eq. (12), the critical crack depth can be obtained by setting $K_{\max}$ equal to the fracture toughness K_C [28, 29]:

$$a_C = \left(\frac{K_C}{Y\sigma_{\max}} \right)^2 / \pi \tag{20}$$

where $\sigma_{\max}$ is the maximum stress under one simulated rainfall time period t.

The obtained average stress range $\Delta\sigma$ and the critical crack depth a_c are then substituted into Eq. (18) to calculate the number of allowable cyclic stress N_c. Assuming the fatigue damage is linearly accumulated for multiple simulated rainfall times, the duration of the MLR increasing period under low rain intensities can be calculated as

$$t_{MLR} = \frac{N_c}{N_t} t \tag{21}$$

where N_c is the allowable number of stress cycles till the end of crack propagation under low rain intensities, N_t is the applied number of stress cycles in one simulated rainfall time t. Accuracy

results when using this approximation for calculating fatigue life under low rain intensities are discussed in Section 4.3.

2.3.3 Fatigue life calculation for wind turbine blade coating

The total fatigue life, t_I, under a rain intensity at each element of the FEA model is calculated by adding the fatigue life during the incubation period and the fatigue life during the MLR increasing period, expressed as

$$t_I = t_{incubation} + t_{MLR} \tag{22}$$

where $t_{\text{incubation}}$ and t_{MLR} are obtained by Eqs. (9) and (21), respectively. In the studied WTB coating, as the crack grows, adjacent crack tips may interact with each other causing the crack propagation path to bend and the cracks to merge. According to Li et al. [35], when the cracked area accounts for 78% ~ 90% of a coating material, the cracks start to merge and the coating enters into a rapid failure stage. Here, the 84$^{\text{th}}$ percentile (center of the 78% to 90% from Li et al. [35]) of the total fatigue life of all FEA elements is selected as the fatigue life of the WTB coating.

Combining the PMF P_{I} of the rain intensity and the total rainfall hours per year t_A at a WT location, the accumulated fatigue damage of the WTB coating per year $D_{1\text{year}}$ considering different rain intensities can be calculated as

$$D_{1\text{year}} = \sum_I \frac{P_I \times t_A}{t_I} \tag{23}$$

Thus, the expected fatigue life t_f of the WTB coating can be calculated as

$$t_f = \frac{1}{D_{1\text{year}}} \tag{24}$$

3 CASE STUDY

The proposed computational framework is applied in the fatigue life evaluation of a composite panel at the tip section of a blade leading edge. The composite panel is modelled in the FEA analysis as a layup that consists of a coating layer, a composite layer beneath the coating layer, a foam core material layer in the middle, and another composite layer at the bottom (Fig. 5). The coating material is an epoxy gelcoat, as specified in the Sandia 100-meter all-glass baseline WTB [36] and has a thickness of 0.6 mm. Each composite layer consists of the composite material QQ1, which is a glass-fiber-reinforced plastic (GFRP) laminate that consists of Vantico TDT 177-155 Epoxy Resin, Saertex U14EU920-00940-T1300-100000 0's, and VU-90079-00830-01270-000000 45's fabrics [37]. The core material is selected to be Corecell^{TM} M-Foam M200 [38]. Detailed material properties are provided in Table 1.

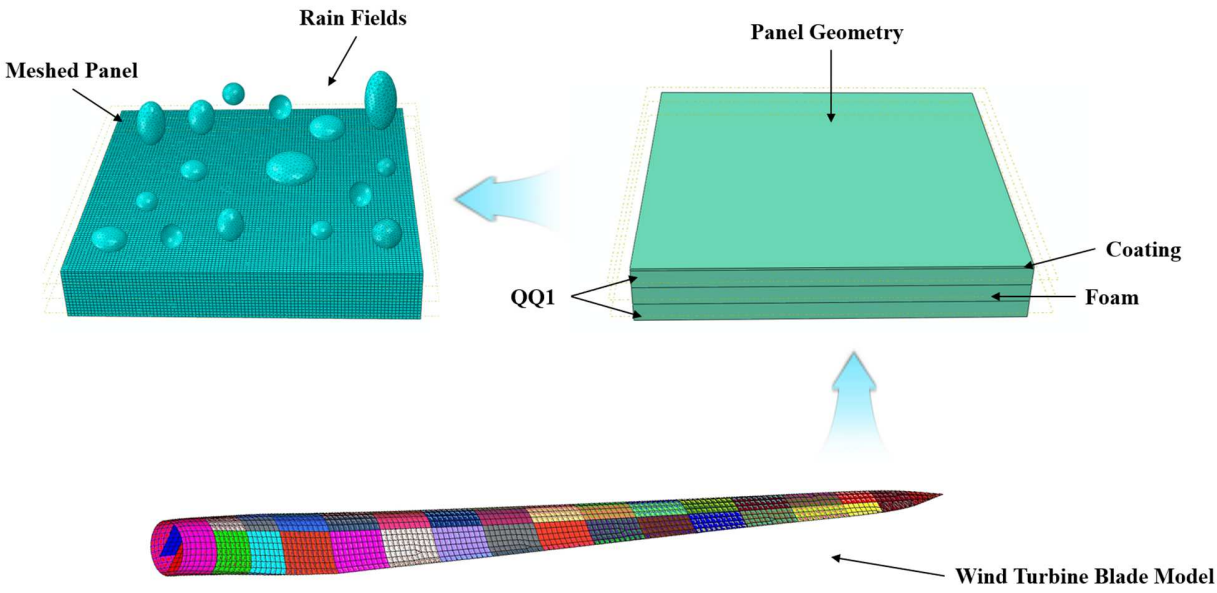

Figure 5 Schematic diagram of raindrops impacting on the panel at the tip of a wind turbine blade.

428 **Table 1** Material properties of the composite panel used in the FEA model [36]

Material Properties \ **Material Types**	Coating	QQ1	Foam
Longitudinal Young's modulus E_1 (GPa)	3.44	33.1	0.256
Transversal Young's modulus E_2 (GPa)	3.44	17.1	0.256
Poisson's ratio v_{12}	0.3	0.27	0.33
Shear modulus G_{12} (GPa)	1.38	6.29	0.098
Density ρ (kg/m^3)	1235	1919	200

429 The dimension of the simulated blade panel is 100 × 100 × 15.6 mm. The boundary condition
430 is set to fixing the bottom surface of the panel as a typical approach for raindrop impact simulation
431 [11, 27]. Two assumptions are made here: 1) the layers in the sandwich panel are perfectly bonded,
432 as the consideration of cohesive property between layers would complicate the stress analysis; 2)
433 the effect of the blade surface curvature on the impact stress is not considered in this case study.
434 There are 10000, 50000, and 50000 SC8R elements are used to mesh the coating layer, each of the
435 composite layer, and the foam layer, respectively (Fig. 5). SC8R is an 8-node, quadrilateral, first-
436 order interpolation, stress/displacement continuum shell element with reduced integration. The
437 average mesh size of the SPH particles in a raindrop is 0.1 times the diameter of the raindrop. The
438 total number of SPH particles is ~750 – 1100 depending on different raindrop sizes and shapes.
439 These numbers of the SC8R elements and the SPH particles are determined based on the sensitivity

440 analyses of different mesh sizes on the calculated stress results and the affordable computational
441 time in this case study.

442 The proposed computational framework is validated by comparing the fatigue life of the
443 studied WTB tip panel under different rain intensities with Bech's results in [8] with the same
444 impact speed of 90 ms^{-1}. In addition, based on the rainfall statistics data in Miami, FL, from August
445 1957 to August 1958 [39], the PMF of the rain intensity is created (see Figure 6) and used to
446 calculate the fatigue life of the studied panel. Detailed results and discussion are provided as
447 follows.

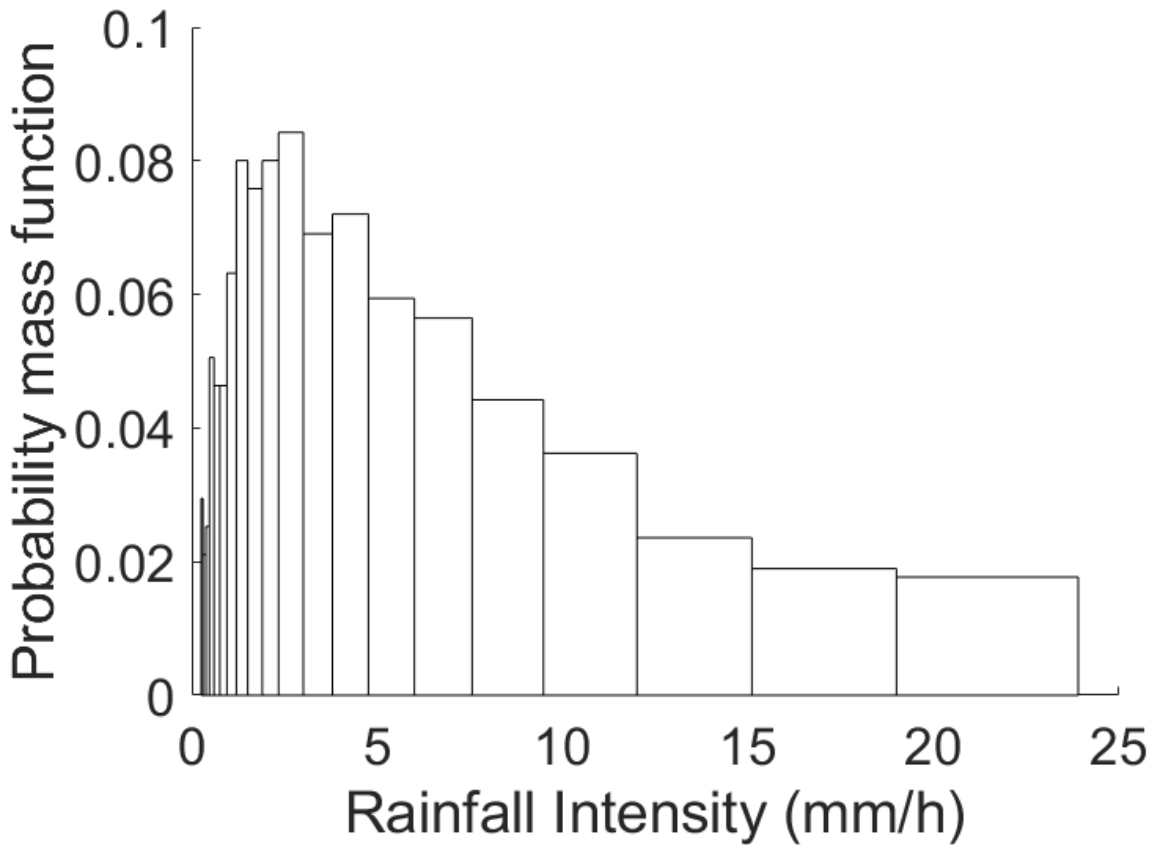

448

449 **Figure 6** The probability mass function of rain intensity in Miami, FL, from August 1957 to
450 August 1958

4 RESULTS AND DISCUSSION

4.1 Extended Stochastic Rain Fields

As a demonstration, Fig. 7 shows the top views of the extended stochastic rain fields with varying raindrop shapes and sizes under four rain intensities, 1 mm h^{-1}, 10 mm h^{-1}, 20 mm h^{-1}, and 50 mm h^{-1}. The flat ellipsoid, spindle ellipsoid, and spherical raindrops are indicated by red, green, and blue solid circles, respectively. This figure clearly visualizes that as the rain intensity increases the number and the size of raindrops increase accordingly. Because this research focuses on the WTB coating stress and fatigue due to the raindrop impact, as elaborated in Sections 4.2 and 4.3, the complex mutual interaction and dynamic deformation of raindrops during their falling are not considered here.

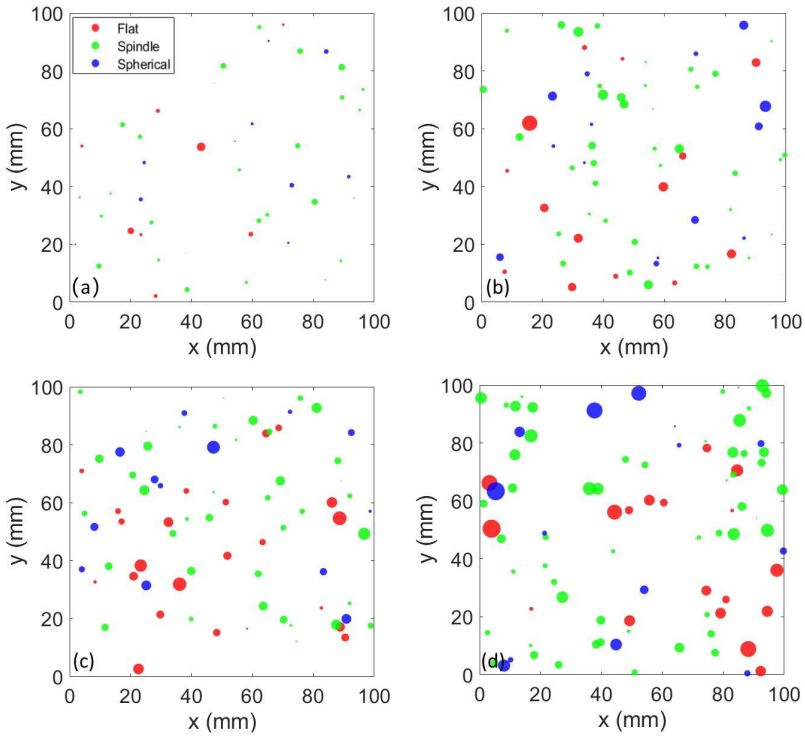

Figure 7 Simulated stochastic rain fields under four rain intensities: (a) 1 mm h^{-1}, (b) 10 mm h^{-1}, (c) 20 mm h^{-1}, and (d) 50 mm h^{-1}.

4.2 Raindrop Impact Stress

The stress waves due to raindrop impact is first investigated. Figures 8 and 9 demonstrate the propagation of von Mises stress of the panel under a single spherical raindrop impacting at the panel center with 90° impact angle. The raindrop diameter is 2 mm, and the impact speed is 90 ms^{-1}. As a result of the impact, there is a Rayleigh wave generated and propagated from the impact center to the free boundary of the coating surface (Fig. 8). In addition, the impact produces longitudinal and transverse body waves that accompany stress variation inside the panel exhibiting an interference field of these waves (Fig. 9).

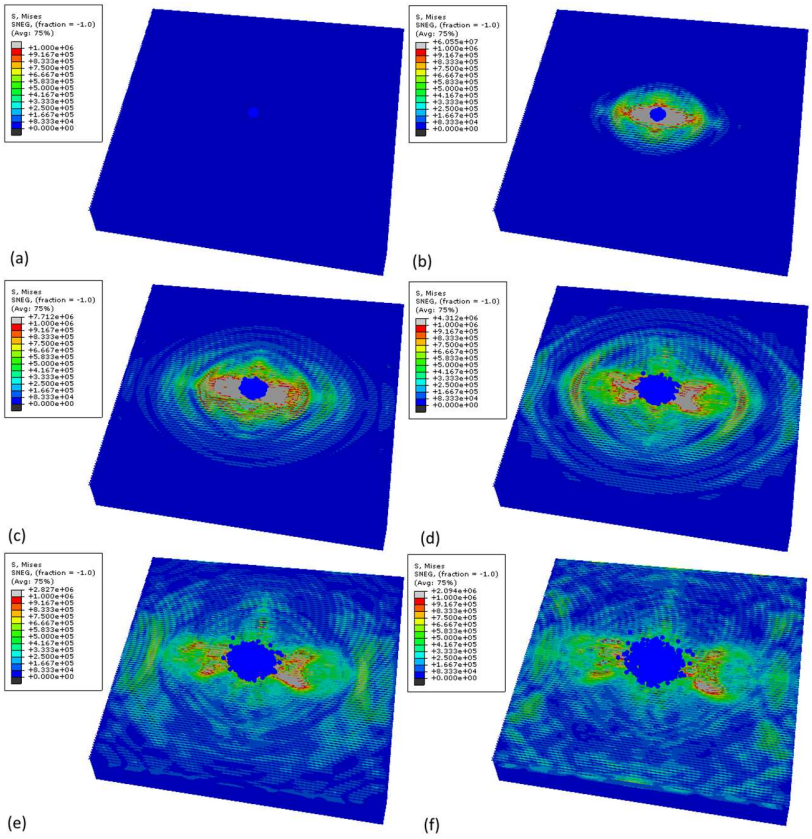

Figure 8 Simulation of a single raindrop impact. (a-f) von Mises stress contours of the top coating at six time instants (0 µs, 10 µs, 20 µs, 30 µs, 40 µs, 50 µs) using the raindrop diameter of 2 mm and the impact speed of 90 ms^{-1}.

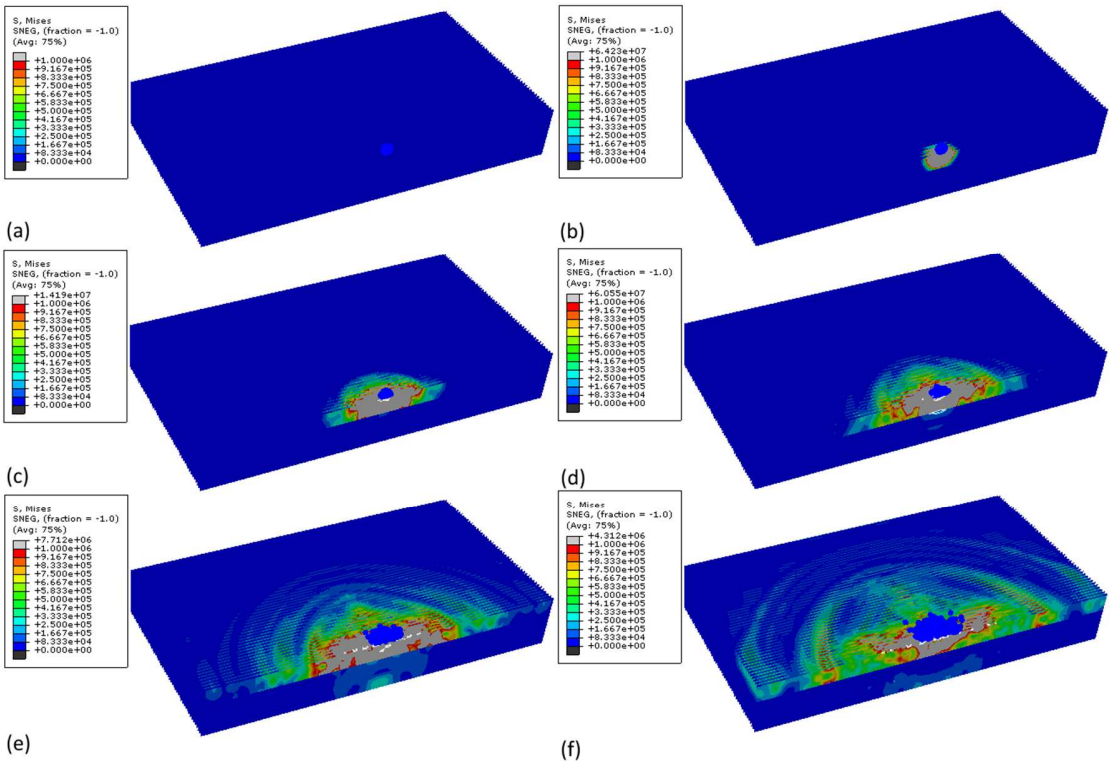

Figure 9 Simulation of a single raindrop impact. (a-f) cross-sectional views of von Mises stress contours at six time instants (0 µs, 1 µs, 5 µs, 10µs, 20 µs, 30 µs) using the raindrop diameter of 2 mm and the impact speed of 90 ms^{-1}.

Two high-stress regions are observed during the raindrop impact process: the one occurring at the raindrop-coating contact surface (Figs. 8(b-f)) and the other is propagating through the thickness below the surface (Figs. 9(a-f)). The former is due to the raindrop peak impact pressure acting as the primary wave source, while the latter is caused by superposition of the stresses initiated from the shock wave front in the raindrop and from the high-pressure point. These findings further confirm that micro-crack/fatigue is possibly occurring both at the raindrop-coating contact surface and underneath the coating.

It is worth noting that there is a clear stress interface between the QQ1 layer and the foam layer (Figs. 9(b-f)) due to the different elastic material properties of the two layers. Under the

assumption of perfectly bonded layers, the elastic deformation of QQ1 and foam layer is the same in the interfaces between layers. As the Young's modulus of the foam layer is much lower than that of the QQ1 layer (see Table 1), the stresses in the foam layer are much lower than those in the QQ1 layer. This finding confirms that the foam layer plays a vital role as a stress cushion in composite WTBs.

The influence of the raindrop size, impact speed, impact angle, and raindrop shape on the stress evolution on the impacted coating is shown in Fig. 10. The coating center element with the highest von Mises stress is studied here. Figure 10(a) shows the von Mises stress induced by the normal impact (90º) under the same impact speed (90 ms^{-1}) and different spherical raindrop diameters (1 mm, 2 mm, and 5 mm). A clear two-peak mode is observed for the stress time series of all three cases, which is in line with earlier observations [5]. The gap between the two peaks is increased as the raindrop size increases (Fig. 10(a)). The first stress peak is due to the direct impact of the raindrop against the coating surface, while the second stress peak may be generated by the shock wave front after the high density liquid region is created [40].

Figure 10(b) compares the von Mises stress under the normal impact (impact angle 90º) of a spherical raindrop (diameter 2 mm) with three different impact speeds (70 ms^{-1}, 90 ms^{-1}, and 100 ms^{-1}). It is found that three first stress peaks (44 MPa, 64 MPa, and 86 MPa) increase as the impact speed increases. The ratio among the three first-peak von Mises stresses is approximately closed to the ratio among the square of the impact speeds, which is consistent with the relationship between the kinetic energy and the impact speed of the raindrop. However, the second stress peak is not significantly influenced by the impact speed as shown in Fig. 10(b).

To investigate the influence of the impact angles on the stress, a spherical raindrop with diameter of 2 mm and impact speed of 90 ms^{-1} is used to impact the blade panel with three different

impact angles (30º, 60º, and 90º). Figure 10 (c) shows that, as the impact angle decreases, the stress is dramatically reduced, especially for the first peak stress, which indicates that non-perpendicular raindrop impact could significantly reduce the impact stress.

Figure 10(d) compares the von Mises stress under three different raindrop shapes (flat, spindle, spherical) with the same volume ($4/3\times\pi\times4^3$ mm^3) and the impact speed (90 ms^{-1}). For the non-spherical raindrops (spindle and flat), the two stress peaks are not as obvious as those due to the spherical raindrop. Instead, the stress corresponding to the non-spherical raindrops have a large fluctuation in the time series. In addition, the spindle raindrop creates the maximum first-peak and longest fluctuating time among the three raindrop shapes, while the flat raindrop generates smaller stress fluctuation than those by the other two counterparts, as demonstrated in Fig. 10(d).

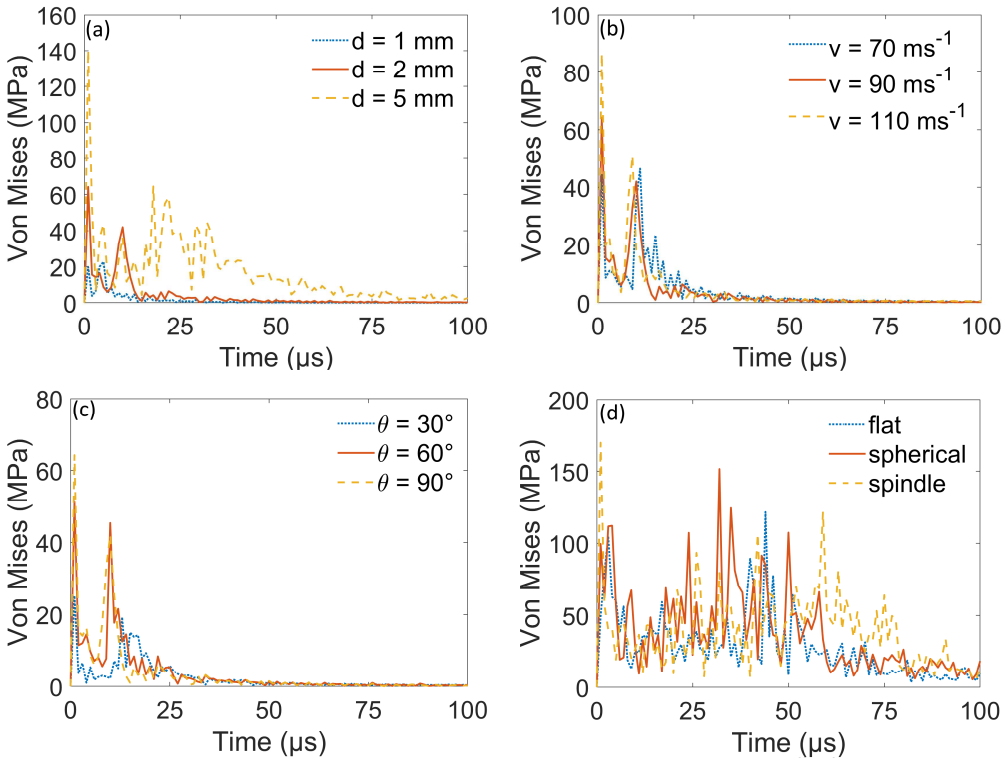

Figure 10 Comparison of coating von Mises stress considering different (a) raindrop sizes, (b) impact speeds, (c) impact angles, and (d) raindrop shapes.

The accuracy of the stress interpolation method proposed in Section 2.2.2 is verified by comparing the interpolated impact stress with the stress directly calculated using the SPH approach. As a demonstration, Fig. 11 shows an interpolated stress when a 2.5 mm diameter spherical raindrop impact at the top-right corner of the blade panel with an impact angle of 80° and an impact speed of 90ms^{-1}. Taking the center of the panel as the origin of the coordinate system, the impact point is at (28 mm, 28 mm). The four closest cases are (spherical, d = 2 mm, θ = 75°, v = 90 ms^{-1}), (spherical, d = 2 mm, θ = 90°, v = 90 ms^{-1}), (spherical, d = 3 mm, θ = 75°, v = 90 ms^{-1}) and (spherical, d = 3 mm, θ = 90°, v = 90 ms^{-1}). Figure 11(a) compares the time series of interpolated von Mises stress of the raindrop and those of the closes four raindrop impact cases. As illustrated in Fig. 11(b), it is observed that the interpolated stress agrees well with the stress directly calculated by the SPH approach.

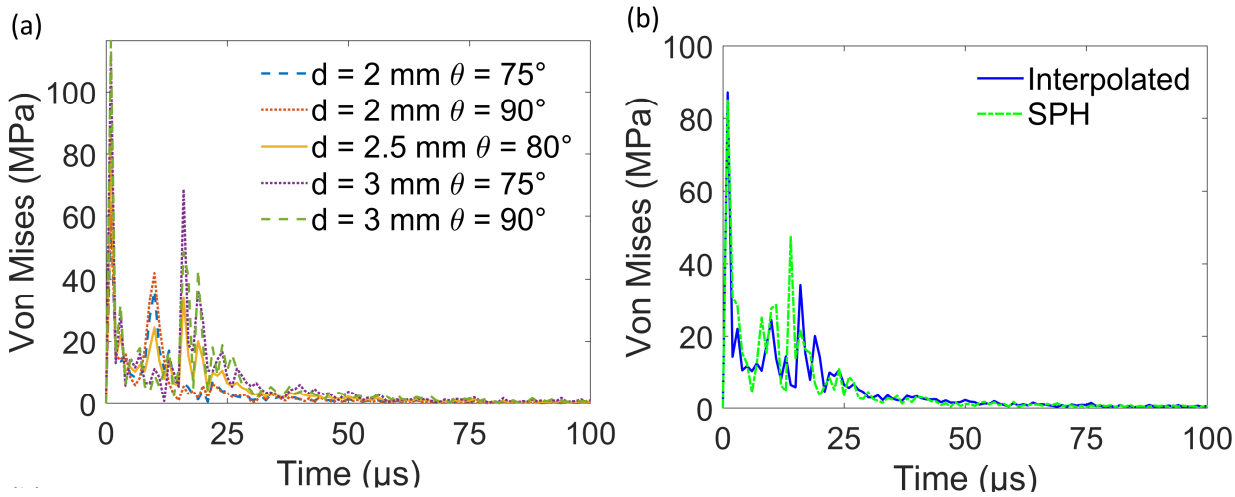

Figure 11 Interpolated impact stress due to a random raindrop (diameter d = 2.5 mm, spherical shapes, impact angles θ = 80°, impacting at a top-right corner of the blade panel. (a) Comparison of the interpolated impact stress and the stresses of the four closet raindrop impact cases; (b) Comparison of interpolated stress (blue solid curve) and the SPH stress (green dash-dotted curve)

4.3 Blade Coating Fatigue

The accuracy of the proposed equivalent crack propagation method is first verified by comparing fatigue life during the MLR increasing period based on the equivalent crack propagation method and the traditional crack propagation method, as shown in Table 2. Under large rain intensities (11 mm $h^{-1} \leq I \leq 20$ mm h^{-1}), the relative error using the equivalent crack propagation method is less than 3% and decreases as the rain intensity decreases, while the computational time using the equivalent crack propagation method is significantly smaller than that using the traditional method. For example, the smallest relative error using the equivalent crack propagation method when rain intensity equals to 11 mm h^{-1} is only 0.06%, and the computational time using the traditional method is 718.3 times as high as that using the equivalent crack propagation method. Therefore, when the rain intensity is low (i.e., $I \leq 10$ mm h^{-1} in this paper), the equivalent crack propagation method could indeed accurately and efficiently predict the fatigue life during the MLR increasing period.

562 **Table 2** The fatigue life of the blade panel during the MLR increasing period calculated by the
563 crack propagation method and the equivalent crack propagation method under large rain intensities
564 (11 mm $h^{-1} \leq I \leq 20$ mm h^{-1}).

Rain intensity I (mm h^{-1})	The crack propagation method		The equivalent crack propagation method		Relative error $\varepsilon = \lvert t_{f1} - t_{f2} \rvert / t_{f1}$	Computational time ratio t_{c1}/ t_{c2}
	Fatigue lifetime t_{f1} (min)	Computational time t_{c1} (min)	Fatigue lifetime t_{f2} (min)	Computational time t_{c2} (min)		
20	209	108.8	203	6.4	2.87%	17.0
19	372	347.8	366	4.5	1.61%	77.3
18	450	403.0	446	4.9	0.89%	82.2
17	781	566.4	776	3.4	0.64%	166.6
16	874	583.5	869	3.9	0.57%	149.6
15	1831	728.7	1823	3.2	0.44%	227.7
14	2637	1163.8	2631	5.9	0.23%	197.3
13	2687	1212.6	2674	4.8	0.48%	252.6
12	4541	1506.5	4538	3.0	0.07%	502.2
11	8168	1939.3	8163	2.7	0.06%	718.3

565 The influence of the rain intensity, raindrop impact speed, raindrop impact angle, and
566 raindrop shape on fatigue life are investigated. The fatigue life of the coating during the incubation
567 period, the MLR increasing period, and the total fatigue life (summation of the incubation period
568 and the MLR increasing period) under different rain intensities, raindrop impact speeds, raindrop
569 impact angles, and raindrop shapes are provided in Table 3 and depicted in Fig. 12.

570

571 **Table 3** Coating fatigue life under different rain intensities, impact speeds, impact angles, and
572 raindrop shapes

Fixed rain parameters	Varied rain parameters		Incubation period (h)	MLR Increasing period (h)	Total Fatigue Life (h)
Impact Speed=90m/s Impact Angle=90° Raindrop Shape=spherical	Rain Intensity	1 mm/h	10350.00	24966.67	35316.67
		5 mm/h	1.53	12.50	14.03
		10 mm/h	0.52	0.17	0.69
		15 mm/h	0.28	0.10	0.38
		20 mm/h	0.18	0.08	0.26
Rain Intensity=5mm/h Impact Angle=90° Raindrop Shape=spherical	Impact Speed	70 m/s	24.36	357.33	381.69
		80 m/s	2.44	68.63	71.07
		90 m/s	1.53	12.50	14.03
		100 m/s	0.73	1.28	2.01
		110 m/s	0.57	0.15	0.72
Rain Intensity=5mm/h Impact Speed=90m/s Raindrop Shape=spherical	Impact Angle	15°	258.33	1620.00	1878.33
		30°	57.24	610.00	667.24
		45°	15.11	206.17	221.28
		60°	1.77	55.17	56.94
		75°	1.20	10.15	11.35
		90°	1.53	12.50	14.03
Rain Intensity=5mm/h Impact Speed=90m/s Impact Angle=90°	Raindrop Shape	Flat	1.72	37.51	39.23
		Spherical	1.53	12.50	14.03
		Spindle	0.55	0.15	0.7

573 Figure 12(a) compares the fatigue life of the blade coating under the same vertical impact
574 (impact angle = 90º), the impact speed of 90 ms^{-1}, and the spherical raindrops with five different
575 rain intensities (1 mm/h, 5 mm/h, 10 mm/h, 15 mm/h, and 20mm/h). As expected, the fatigue life
576 of the coating decreases exponentially with the increase of the rainfall intensity. It is interesting to
577 find that under low rain intensity (e.g., $I < 7\sim8$ mm/h) the incubation period is shorter than the
578 MLR increasing period, while it becomes longer than the MLR increasing period under large rain
579 intensity (e.g., $I \geq 10$ mm/h). This is probably due to that severer impact stress, consequently
580 severer crack propagation, occurs under larger raindrop size (see Fig. 10(a)) and more raindrops
581 hitting at large rain intensity than that at small rain intensity. This finding also indicates that a rain
582 event with a large rain intensity could more detrimentally influence the blade coating crack
583 propagation than the crack initiation.

584 Figure 12(b) compares the fatigue life of the blade coating under the same rain intensity (5
585 mm/h) and the vertical impact (impact angle = 90º) of spherical raindrops with five different
586 impact speeds (70 ms^{-1}, 80 ms^{-1}, 90 ms^{-1}, 100 ms^{-1}, and 110 ms^{-1}). There is a significantly large
587 gap between the incubation period and the MLR increasing period at the impact speed of 70 ms^{-1},
588 which means the MLR increasing period dominates the total fatigue life under small impact speeds.
589 This gap is narrowed down as the impact speed increases. The current finding also indicates that
590 the raindrop impact speed influences the MLR increasing period more severe than incubation
591 period.

592 Figure 12(c) compares the fatigue life of the blade coating under the same rain intensity (5
593 mm/h) and impact speed (90 ms^{-1}) of spherical raindrops with five different impact angles (15º,
594 30º, 45º, 60º, 75º, and 90º). The fatigue life during the MLR increasing period dominates the total

595 fatigue life under small impact angle. As the impact angle increases, both the fatigue life during
596 the incubation period and the MLR increasing period are exponentially decreasing.

597 Figure 12(d) compares the fatigue life of the blade coating under the same rain intensity (5
598 mm/h), impact speed (90 ms^{-1}) and the vertical impact (impact angle = 90º), but three different
599 raindrop shapes (flat, spherical, spindle). It is interesting to find that 1) under the flat raindrops the
600 MLR increasing period is 21.8 times longer than the incubation period; 2) the MLR increasing
601 period under the flat raindrops is 250.1 times longer than that under the spindle raindrops. These
602 could be probably because the spindle raindrops cause larger stress peak and longer stress
603 fluctuation than those caused by the flat raindrops (see Fig. 10(d)).

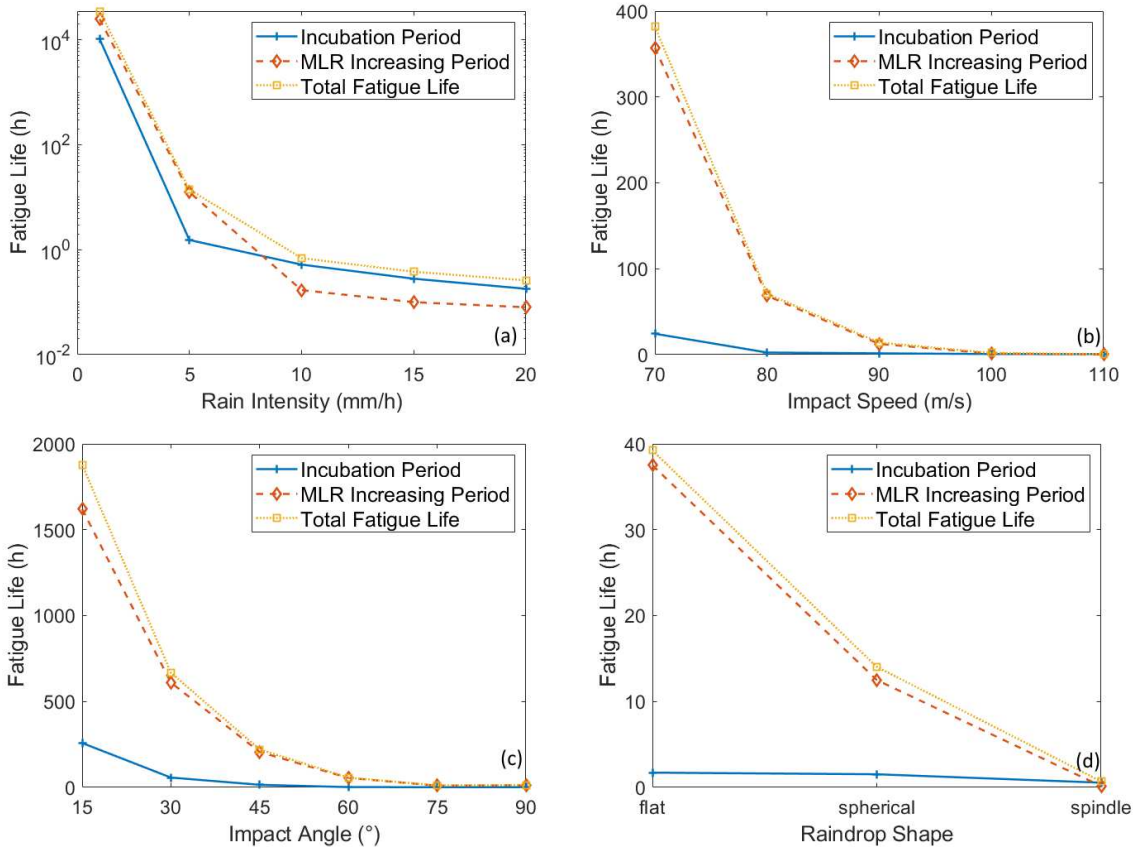

604

605 **Figure 12** Coating fatigue life corresponding to different (a) rain intensities, (b) impact speeds,
606 (c) impact angles, and (d) raindrop shapes.

To further verify the accuracy of the proposed computational framework, the calculated total fatigue life of the blade coating is compared with that obtained by Bech et al. [8] under the same impact speed of 90 ms^{-1}. Table 4 compares the total fatigue life under five rain intensities (20 mm h^{-1}, 10 mm h^{-1}, 5 mm h^{-1}, 2 mm h^{-1}, and 1 mm h^{-1}). In this table, the hours per year indicate the number of hours corresponding to the rain intensity in a year, which is from Bech et al. [8]. The faction of life spent per year equals the hours per year divided by the calculated total fatigue life. The reciprocal of the sum of fraction is obtained as the expected life in year. In general, the total fatigue life under the five rain intensities are longer than those obtained by Bech et al. [8]. Using the same rain hours per year data, the expected fatigue life using the proposed framework is 2.1 years which is slightly longer than that obtained by Bech et al. [8]. This longer fatigue life is mainly because the proposed framework involves more sophisticated and realistic computational approaches. For example, the extended stochastic rain field simulation considers various impact angles and raindrop shapes that may alleviate the calculated stress compared with that obtained by assumed vertical impact of all perfectly spherical and fixed-diameter raindrops used in Bech et al. [8]. Given that very few WTB rain erosion experimental data are available in literature, this comparison still shows that the proposed computational framework could produces reasonable rain-erosion fatigue life for WTBs. It is worth noting that the fatigue life here is based on the assumption that the blade is under continuous raindrop impact throughout its service life and could be conservative.

629 **Table 4** Comparison of the total fatigue life in this study and from Bech's result under different
630 rain intensities

Rain intensity (mm h^{-1})	Hours per year (h yr^{-1})	Blade tip speed (m s^{-1})	Total fatigue life (Bech's result) (h)	Fraction of life spent per year (Bech's result) (%)	Total fatigue life (this study) (h)	Fraction of life spent per year (this study) (%)
20	1.8	90	3.5	51	4.2	42.9
10	8.8	90	79	11	192.7	4.6
5	88	90	3600	2.4	14463	0.6
2	263	90	7.5×10^{5}	3.5×10^{-2}	1.6×10^{6}	1.6×10^{-2}
1	438	90	2.8×10^{9}	1.6×10^{-5}	4.5×10^{7}	9.7×10^{-4}
Sum of fraction (%):				64.4		48.1
Expected life (year):				1.6		2.1

631

632 Based on the rainfall statistics data in Miami, FL, from August 1957 to August 1958 [39],
633 the rain-erosion fatigue life of the Sandia 100-meter all-glass baseline WTB is ~ 1.3 years using
634 the proposed computational framework and the above expected fatigue life calculation method.
635 This indicates the necessity of the blade surface repairing as early as 1.3 years after installation.

5 CONCLUSIONS

For analyzing WTB coating fatigue due to rain erosion, this paper presents a state-of-the-art computational framework that including an extended stochastic rain field simulation (considering varied raindrop sizes, impact speeds, impact angles, and raindrop shapes), SPH-and-interpolation hybrid raindrop impact stress calculation, and coating fatigue analysis (considering both the incubation period and the MLR increasing period for the first time). Based on this new framework, some interesting results are obtained and summarized as follows:

1) Both surface Rayleigh wave and longitudinal and transverse body wave of impact stress are generated by raindrop impact accompany with high-stress regions during the propagation of these stress waves in the WTB.
2) The influence study of the raindrop size, impact speed, impact angle, and raindrop shape on the stress evolution on the impacted coating shows that the inclined impact of flat-ellipsoid raindrops could produce smaller stress fluctuation than the vertical impact of spindle-ellipsoid raindrops do.
3) The proposed stress interpolation method and the equivalent crack propagation method could efficiently and accurately calculate the impact stress and fatigue, respectively, under a stochastic rain event.
4) The influence study of the rain intensity, impact speed, impact angle, and raindrop shape on the fatigue life reveals that i) a rain event with a large rain intensity could more detrimentally influence the blade coating crack propagation than the crack initiation; ii) the MLR increasing period dominates the total fatigue life under small impact speeds (e.g., 70 m/s) and the raindrop impact speed influences the MLR increasing period more severe than incubation period; iii)

658 the vertical impact of spindle-ellipsoid raindrops could cause significantly larger fatigue
659 damage than the inclined impact of flat-ellipsoid raindrops do.
660 5) The proposed framework is verified by comparing the calculated fatigue life with existing
661 results in literature, and is readily applicable to predict WTB coating fatigue life due to rain
662 erosion given rainfall statistic data at a location.

663 Although the current research provides innovative contributions for predicting the WTB
664 coating fatigue life due to rain erosion, limitations and future work may include:

665 1) The usage of the proposed framework for WTB design and maintenance has not be investigated
666 in this paper. Future work may be the application of the framework to design of new WTB
667 coating and to optimal control of wind turbine rotation to reduce the rain erosion for WTB, as
668 well as to predictive maintenance (for example, determine the time when the predictive
669 maintenance due to rain erosion is necessary based on the fatigue damage calculated by the
670 proposed framework).
671 2) The rain-wind correlation, the moisture effect, the chemical corrosion from insects, and other
672 object impacts (e.g., atmospheric particles, hail, and sand) have not considered in this paper.
673 WT damage calculation considering these factors and the validation with real experimental
674 results are worth investigating in the future.

675

REFERENCES

1. Woods, R.D., Screening of surface waves in soils. J. Soil. Mech. Found. Div., 1968. **94**: p. 951-980.
2. Busch, H., G. Hoff, G. Langbein, Geoffrey Taylor, D. C. Jenkins, M. A. Taunton, A. A. Fyall, R. F. Jones, and T. W. Harper., Rain erosion properties of materials. Philosophical Transactions for the Royal Society of London. Series A, Mathematical and Physical Sciences, 1966. **1110**: p. 168-181.
3. Heymann, F.J., High-speed impact beteen a liquid drop and a solid surface. J. Appl. Phys., 1969. **40**: p. 5113-5122.
4. Dear, J.P. and J.E. Field, High-speed photography of surface geometry effects in liquid/solid impact. J. Appl. Phys., 1988. **63**: p. 1015-1021.
5. Amirzadeh, B., et al., A computational framework for the analysis of rain-induced erosion in wind turbine blades, part I: Stochastic rain texture model and drop impact simulations. Journal of Wind Engineering and Industrial Aerodynamics, 2017. **163**: p. 33-43.
6. Villermaux, E. and B. Bossa, Single-drop fragmentation determines size distribution of raindrops. Naturey Physics, 2009. **5**: p. 697-702.
7. Bartolomé, L. and J. Teuwen, Prospective challenges in the experimentation of the rain erosion on the leading edge of wind turbine blades. Wind Energy, 2019. **22**: p. 140-151.
8. Bech, J.I., C.B. Hasager, and C. Bak, Extending the life of wind turbine blade leading edges by reducing the tip speed during extreme precipitation events. Wind Energy Science, 2018. **3**: p. 729-748.
9. Eisenberg, D., S. Laustsen, and J. Stege, Wind turbine blade coating leading edge rain erosion model: Development and validation. Wind Energy, 2018. **21**: p. 942-951.
10. Slot, H.M., et al., Leading edge erosion of coated wind turbine blades: Review of coating life models. Renewable Energy, 2015. **80**: p. 835-848.
11. Amirzadeh, B., et al., A computational framework for the analysis of rain-indcued erosion in wind turbine blades, part II: Drop impact-indcued stresses and blade coating fatigue life. Journal of Wind Engineering and Industrial Aerodynamics, 2017. **163**: p. 44-54.
12. Springer, G.S. and C.I. Yang, Model for the Rain Erosion of Fiber Reinforced Composites. AIAA Journal, 1975. **13**(7): p. 877-883.
13. C M Preece, a. and N.H. Macmillan, Erosion. Annual Review of Materials Science, 1977. **7**(1): p. 95-121.
14. Verma, A.S., et al., Leading edge erosion of wind turbine blades: Effects of blade surface curvature on rain droplet impingement kinematics. Journal of Physics: Conference Series, 2020. **1618**.
15. Thomas, G.P., J.H. Brunton, and D. Tabor, Drop impingement erosion of metals. Proceedings of the Royal Society of London. A. Mathematical and Physical Sciences, 1970. **314**(1519): p. 549-565.
16. Hu, W., et al., A computational model of wind turbine blade erosion induced by raindrop impact. Journal of Physics: Conference Series, 2020. **1452**: p. 012048.
17. Beard, K.V., V.N. Bringi, and M. Thurai, A new understanding of raindrop shape. Atmospheric Research, 2010. **97**(4): p. 396-415.
18. Keegan, M.H., D.H. Nash, and M.M. Stack, On erosion issues associated with the leading edge of wind trubine blades. Journal of Physics D: Applied Physics, 2013. **46**: p. 383001.
19. Best, A.C., The size distribution of raindrops. Quarterly Journal of the Royal Meteorological Society, 1950. **76**(327): p. 16-36.
20. McTaggart-Cowan, J.D. and R. List, Collision and Breakup of Water Drops at Terminal Velocity. Journal of the Atmospheric Sciences, 1975. **32**(7): p. 1401-1411.

21. Gunn, R. and G.D. Kinzer, THE TERMINAL VELOCITY OF FALL FOR WATER DROPLETS IN STAGNANT AIR. Journal of Meteorology, 1949. **6**(4): p. 243-248.

22. Johnson, R.J., R.A. Stryk, and S.R. Beissel, SPH for High Velocity Impact Calculations. Computer Methods in Applied Mechanics and Engineering, 1996. **139**: p. 347-373.

23. Colagrossi, A. and M. Landrini, Numerical Simulation of Interfacial Flows by Smoothed Particle Hydrodynamics. Journal of Computational Physics, 2003. **191**(2): p. 448-475.

24. Gingold, R.A. and J.J. Monaghan, Smoothed Particle Hydrodynamics: Theory and Application to Non-Spherical Stars. Monthly Notices of the Royal Astronomical Society, 1977. **181**: p. 375-389.

25. Keegan, M.H., Wind Turbine Blade Leading Edge Erosion: An Investigation of Rain Droplet and Hailstone Impact Induced Damage Mechanisms. 2014, University Of Strathclyde.

26. Astrid, B., Investigation of Droplet Erosion for Offshore Wind Turbine Blades. Ann. Acad. Med. Stetin., 2014. **59**(1): p. 170-171.

27. Verma, A.S., et al., Numerical investigation of rain droplet impact on offshore wind turbine blades under different rainfall conditions: A parametric study. Composite Structures, 2020. **241**.

28. Stephens, R.I., Metal Fatigue in Engineering. 1980, New York： Wiley,1980.

29. Chen, C., Fatigue and Fracture. 2002, Wuhan:Huazhong University of Science and Technology PressS.

30. C.M. Manjunatha, A.C.T., A.J. Kinloch, S. Sprenger,, The tensile fatigue behaviour of a silica nanoparticle-modified glass fibre reinforced epoxy composite. Composites Science and Technology,, 2010. **70**(1): p. 193-199.

31. ASTM, C., Standard Practices for Cycle Counting in Fatigue Analysi. 2005: ASTM International, West Conshohocken.

32. Paris, P., A Critical Analysis of Crack Propagation Laws Journal of basic engineering, 1963. **85**(4): p. 528.

33. Brown, E.N., S.R. White, and N.R. Sottos, Fatigue crack propagation in microcapsule-toughened epoxy. Journal of Materials Science, 2006. **41**(19): p. 6266-6273.

34. Doagou-Rad, S. and L. Mishnaevsky, Rain erosion of wind turbine blades: computational analysis of parameters controlling the surface degradation. Meccanica, 2019. **55**(4): p. 725-743.

35. Li, C.-J., et al., Evolution of Lamellar Interface Cracks During Isothermal Cyclic Test of Plasma-Sprayed 8YSZ Coating with a Columnar-Structured YSZ Interlayer. Journal of Thermal Spray Technology, 2013. **22**(8): p. 1374-1382.

36. Griffith, D.T. and T.D. Ashwill, The Sandia 100-meter all-glass baseline wnd turbine blade: SNL100-00. 2011, Sandia National Laboratories, Albuquerque, New Mexico, USA.

37. Mandell, J.F. and D.D. Samborsky, SNL/MSU/DOE composite material fatigue database mechanical properties of composite materials for wind turbine blades version 23.0. Montana State University, Bozeman, 2014.

38. Gurit. Structural Core Materials - Gurit Corecell M The Marine Foam (Access on June 21, 2019). Available from: https://www.gurit.com/Our-Business/Composite-Materials/Structural-Core-Materials/Gurit-Corecell-M.

39. Jones, D.M.A. and A.L. Sims, Climatology of Instantaneous Rainfall Rates. Journal of Applied Meteorology, 1978. **17**(8): p. 1135-1140.

40. Zhou, Q., et al., Analysis of water drop erosion on turbine blades based on a nonlinear liquid-solid impact model. International Journal of Impact Engineering, 2009. **36**: p. 1156-1171.

ACKNOWLEDGEMENTS

This work is supported by the National Natural Science Foundation of China (Grant No. 51905475) and the National Key R&D Program of China (Grant No. 2019YFB1705200, 2018YFB1201802-1).

NOMENCLATURE

a	Crack depth
a_0	Initial crack depth
a_c	Critical crack depth
b	Fatigue strength exponent (FSE)
C	Exponential parameter describing the fatigue crack growth performance of the material
d	Raindrop diameter
D	Fatigue damage
D_{1year}	Accumulated fatigue damage of the WTB coating per year
D_s	Damage accumulated over time t_s.
h	Hight of the tall-column
I	Rain intensity in mm h^{-1}
K	Stress intensity factor
K_C	Fracture toughness
K_{max}	Maximum stress intensity factor

780	$K_{\min}$	Minimum stress intensity factor
781	m	Linear parameter describing the fatigue crack growth performance of the material
782	$N(V)$	Number of raindrops in volume V
783	N	The number of stress cycles
784	N_c	Number of allowable cyclic stress till the end of the MLR increasing period
785	N_f	Number of allowable cycles in the S-N method
786	N_t	Applied number of stress cycles in one simulated time t
787	P_I	Probability of the rain intensity I
788	r_0	Equivalent spherical radius
789	R	The ratio of the minimum cyclic stress to the maximum cyclic stress
790	t_A	Total rainfall hours per year at a WT location
791	t_{c1}	Computational time by the crack propagation method
792	t_{c2}	Computational time by the crack equivalent crack propagation method
793	t_f	Expected fatigue life of the WTB coating
794	t_{f1}	Fatigue life during the MLR increasing period by the crack propagation method
795	t_{f2}	Fatigue life during the MLR increasing period by the equivalent crack propagation method
797	$t_{\text{incubation}}$	Fatigue life during the incubation period
798	t_I	Total fatigue life under a rain intensity

799	t_{MLR}	Duration of the MLR increasing period
800	t	Duration of the simulated rain in equivalent crack propagation method
801	t_s	Duration of a simulated rain event
802	T	Duration of the simulated rain event
803	UTS	Ultimate tensile strength
804	v	Impact speed
805	V	Unit volume
806	Y	A dimensionless parameter related to the shape of the crack.
807	α	Axis ratio
808	ΔK	Stress intensity factor range
809	$\Delta\sigma$	Average stress range in equivalent crack propagation method
810	θ	Impact angles
811	λ	Expected number of raindrops per unit volume
812	σ_a	Stress amplitude
813	$\sigma_a^{'}$	Corrected stress amplitude
814	σ_f	Fatigue strength coefficient (FSC)
815	σ_m	Mean stress
816	$\sigma_{\max}$	Maximum stress under one simulated rainfall time period